aerospace

MDPI

Article

Surrogate Model for Lunar Sampling Based on Bayesian Neural Network and Active Learning to Enhance Coring Efficiency

Shuang Li [1,†], Zihao Yuan [1,†], Tao Du [1,2], Renxu Hao [1,3], Haifeng Zhao [1,2,*] and Ke Wang [1]

[1] Key Laboratory of Space Utilization, Technology and Engineering Center for Space Utilization, Chinese Academy of Sciences, Beijing 100094, China
[2] School of Aeronautics and Astronautics, University of Chinese Academy of Sciences, Beijing 100049, China
[3] School of Mechanical Engineering, Hebei University of Science and Technology, Shijiazhuang 050018, China
* Correspondence: hfzhao@csu.ac.cn
† These authors contributed equally to this work.

Abstract: Drilling parameters are intricately linked to the mechanical interactions between the drilling device and lunar regolith, significantly affecting sampling characteristics. Achieving high coring efficiency requires a deep understanding of how these parameters influence the coring rate. While experiments can characterize coring performance, they are time-consuming and costly due to the need for numerous repetitive tests. To address this, this paper integrates experiments with machine learning to develop a surrogate model that replaces experimental results, allowing for extrapolation and interpolation to analyze the sensitivities of drilling parameters. Specifically, Taguchi orthogonal experiments are designed to gather a representative sample set, and a Bayesian neural network (BNN) is employed to create a predictive model which can quantify uncertainty. Active learning is then applied to focus additional sampling on uncertain regions, refining the model iteratively to achieve an accurate approximation of experimental results. This approach reduces the number of experiments needed to develop a high-fidelity surrogate model. Validation results demonstrate strong extrapolation accuracy and generalization, with an R^2 of 0.89 and a *MAPE* of 5.74% on the independent test set. Based on this model, this paper analyzes the influence of drilling parameters on sampling performance, providing insights for optimizing drilling parameters to maximize coring efficiency.

Keywords: lunar regolith sampling; hollow stem auger; design of experiment; surrogate model; Bayesian neural network; active learning; coring efficiency

check for updates

Received: 15 January 2025
Revised: 1 February 2025
Accepted: 5 February 2025
Published: 7 February 2025

Citation: Li, S.; Yuan, Z.; Du, T.; Hao, R.; Zhao, H.; Wang, K. Surrogate Model for Lunar Sampling Based on Bayesian Neural Network and Active Learning to Enhance Coring Efficiency. *Aerospace* **2025**, *12*, 128. https://doi.org/10.3390/aerospace12020128

Copyright: © 2025 by the authors. Licensee MDPI, Basel, Switzerland. This article is an open access article distributed under the terms and conditions of the Creative Commons Attribution (CC BY) license (https://creativecommons.org/licenses/by/4.0/).

1. Introduction

Extraterrestrial regolith contains crucial information about the formation, evolution, and resource deposits of celestial bodies [1,2]. The former Soviet Union, United States, and China, have successively carried out extraterrestrial regolith sample return missions, particularly to the Moon and Mars [3]. The geochemical analysis of these returned samples has deepened humanity's scientific understanding of planetary evolution and the origins of life. The stratigraphic structure of regolith in drilling samples from the lunar subsurface reveals the evolutionary history of celestial bodies, providing greater scientific value than surface samples [4,5]. The hollow stem auger, capable of retrieving regolith samples with continuous stratigraphic information, is the most widely used method for extraterrestrial sampling [6].

Extraterrestrial drilling faces unique technical challenges due to special atmospheric and gravitational conditions. The lack of effective flushing media, such as air or drilling

fluids, complicates chip removal during sampling missions [7,8]. Moreover, the complexity and uncertainty of extraterrestrial regolith further complicate the control of drilling processes [9,10]. In light of these challenges, it is crucial to conduct a systematic investigation of extraterrestrial drilling and sampling characteristics, to identify key control parameters and understand their influence mechanisms, thereby providing the necessary foundation for optimizing drilling parameters to achieve high coring efficiency.

Currently, research on the sampling performance of lunar drilling devices mainly includes theoretical analysis, simulation, and ground-based experiments. In theoretical studies, the interaction between the drill device and the regolith is closely linked to the final coring efficiency, which can be classified into rotational cutting by the drill bit and spiral chip discharge by the drill anger [11]. To investigate the mechanics of cutting model for rotary tool, Armarego et al. [12] proposed a modified thin shear zone mechanics of cutting model, accounting for all the cutting energy and the chip transportation process. The helical-threaded drilling stem can enhance the chip removal performance of the drilling device, operating on principles analogous to screw conveyors commonly employed in powder technology. Yu et al. [13] developed a physical model that links the drive load of the auger to its structural parameters and the characteristics of the conveyed medium. To investigate the complicated relation among the coring rate, the conveying ability of the auger, and drilling parameters such as the penetration and rotation speeds, Chen et al. [14] utilized the Janssen model to establish a coupled drilling–coring dynamics model, which led to a theoretical formula for the coring rate in flexible tube sampling. The aforementioned studies proposed mechanical models for rotational cutting and spiral chip discharge, along with coring performance equations derived from these models. With the advancement of computational techniques, many researchers have conducted studies based on numerical simulations. The Discrete Element Method (DEM) is a numerical simulation method based on the mechanics of discrete media, distinct from continuum mechanics. This method is particularly suited for simulating the particle dynamics of lunar regolith. Wang et al. [15] utilized the DEM to simulate the entire drilling and sampling process by combining the Hertz–Mindlin and bonded contact models. Zhao et al. [16] employed the DEM to simulate the drilling process in lunar soil, analyzing the influence of particle size, position, and shape on the drilling load. Liu et al. [17] employed the DEM to simulate the drilling and coring process in large rock blocks, including simulations of the drill bit and rod penetration, as well as estimates of the drilling load. The aforementioned studies offer valuable insights into drill–regolith interactions and sampling characteristics, yet they face significant limitations when applied to the highly complex scenario of extraterrestrial drilling. Theoretical analysis often relies on simplified assumptions, such as treating regolith as a homogeneous continuum, which overlooks key micromechanical processes like dilatancy and the silo effect [18]. Moreover, numerical simulations depend on accurate in situ data for calibrating physical parameters and boundary conditions, making it challenging to simulate the regolith's geometric distribution and stress variations without such data.

Experiments are the most effective means to simulate real working conditions and the drilling process, providing more reliable sampling results. Nagaoka et al. [19] evaluated the drilling performance of a bidirectional double-helix system, with results showing that an optimal penetration per revolution (*PPR*) can effectively reduce drilling load, improving drilling efficiency. Tang et al. [20,21] used ultrasonic displacement sensors to dynamically monitor core height during drilling, revealing how coring rate and speed varied with depth under different feed-to-rotation ratios. Zhang et al. [22] experimentally investigated the influence of drilling parameters such as drill rod rotating speed and feed rate on sampling characteristics and drilling loads. Wang et al. [23] conducted an orthogonal experiment to study the coupling relationship and impact of drilling parameters on chip removal

performance, providing a ranking of the importance of these parameters. Drilling load responses, such as weight-on-bit (WOB) and torque, reflect the mechanical interaction between the drilling device and regolith, offering critical insights into drilling conditions. Zancy et al. [24] studied various drill bits in a simulated Martian environment, using pressure and torque sensors to analyze WOB and torque variations. Yuan et al. [25] examined the load changes of a dual-screw conveyor drill under different control parameters, finding that penetrating speed and rotating speed ratio have a coupled influence on drilling loads. Gouache et al. [26] proposed a dual-reciprocating drilling method, enhancing efficiency by applying additional downforce, though it compromised core structure preservation. While experiments can most accurately replicate the real drilling process, they are time- and labor-intensive, with limited data acquisition. Moreover, as coring efficiency is influenced by numerous factors, it is difficult to conduct a comprehensive quantitative analysis of the effects of various parameters through experiments alone.

Machine learning algorithms have emerged as powerful tools for identifying underlying patterns in experimental and engineering data, gaining widespread attention in terrestrial drilling. Boukredera et al. [27] utilized Multi-Layer Perceptron, Support Vector Regression (SVR), and Decision Tree Regression to develop predictive models for bit rotation speed, rate of penetration (ROP), and torque. Hao et al. [28] implemented Gradient Boosting Decision Trees to construct an ROP prediction model, further employing Bayesian optimization to identify the optimal combination of drilling parameters. Yang et al. [29] selected Random Forest, Light Gradient Boosting Machine, Extreme Gradient Boosting, and SVR as base learners for ensemble learning, ultimately establishing a predictive model for ROP. Bizhani et al. [30] established a predictive model for ROP using Bayesian neural networks and discussed the sources of uncertainty within a probabilistic framework. As extraterrestrial drilling technology advances, researchers have increasingly turned to machine learning techniques to address challenges within the realm of extraterrestrial drilling. Xu et al. [31] utilized a recurrent neural network to develop a load prediction model for lunar drilling, capable of estimating penetration force and rotational torque in real-time. Liu et al. [32] introduced a real-time temperature prediction model for drilling within simulated lunar regolith by integrating a bidirectional long short-term memory network and self-attention mechanism. Chen et al. [33] used Bayesian linear regression to develop a positioning model for extraterrestrial drilling devices, utilizing the predicted position and the corresponding confidence intervals for error compensation to improve positioning accuracy. Selecting and integrating machine learning algorithms tailored to the specific characteristics of the drilling task and experimental data is crucial for effectively extracting the underlying patterns in drilling data.

To address the high costs of experiments, surrogate models have been developed, leveraging the few samples with machine learning. Surrogate models, also referred to as approximate models, are mathematical representations constructed from a limited set of samples, designed to closely replicate the outcomes of the original model [34]. Given the extended duration and high costs in drilling experiments, machine learning techniques can be employed to construct surrogate models based on the limited sample availability, thus serving as a cost-effective substitute for experiments. Common machine learning algorithms used for surrogate modeling include Kriging, Radial basis function, SVR and artificial neural networks (ANNs) [35]. Notably, ANNs have gained significant attention in surrogate models due to their powerful ability to capture complex, high-dimensional, and nonlinear relationships. For complex systems, it is challenging to construct surrogate models accurately based on single sampling. To address this, active learning (AL) has been proposed, wherein the surrogate model autonomously selects samples that are most likely to improve its performance for further training [36]. Typically, samples with higher

prediction uncertainty are selected during the iterative process for additional sampling, updating the surrogate model to achieve a more precise global approximation. Bayesian neural networks (BNNs), which combine ANN and Bayesian inference, are particularly effective for this purpose, as they not only provide predictions but also quantify the associated uncertainties, making them well-suited for AL processes [37].

To efficiently investigate the coring characteristics and optimize the coring efficiency of lunar drilling devices, this paper proposes a surrogate model for sampling that integrates ground-based experiments with machine learning, serving as a substitute for real-world experiments. Initially, the Taguchi orthogonal design [38] is applied to arrange the drilling experiments, in order to acquire comprehensive and representative samples within a limited number of trials. Subsequently, a BNN is employed to construct the surrogate model, which can quantify the uncertainty of predictions. By integrating an AL strategy, additional sampling is carried out at points with high uncertainty, and the model is iteratively refined to achieve a high-fidelity approximation. Finally, the surrogate model is used to conduct a systematic analysis of the influence and interaction of drilling parameters on coring efficiency. The innovation of this study lies in the introduction of machine learning to uncover patterns in lunar sampling efficiency, constructing a surrogate model to replace experimental results. Additionally, a tailored machine learning approach is designed to address the challenges of high acquisition costs and limited sample sizes in lunar sampling experiments. The structure of this paper is organized as follows: Section 2 presents the design and results of the drilling experiments; Section 3 outlines the process of constructing the surrogate model and evaluates its performance; Section 4 provides an analysis of coring performance based on the surrogate model; and Section 5 concludes this paper.

2. Drilling and Coring Experiments

This section conducts ground-based drilling and sampling experiments under simulated lunar conditions to obtain the quantitative relationship between drilling parameters and coring performance, providing necessary data for the development of the surrogate model. First, the experimental setup is described, including the key characteristics of the simulated lunar regolith and the operational mechanisms of the drilling device. To overcome the high costs associated with experiments, the Taguchi orthogonal method is utilized to optimize the experimental design, facilitating the efficient acquisition of representative samples. The experimental results are then presented, followed by a concise analysis of the findings. Section 2.1 describes the materials and methods used in the drilling experiments, while Section 2.2 presents the experimental results and analysis.

2.1. Experimental Setup

2.1.1. Lunar Regolith Simulant CSU-LRS-1

The physical and mechanical properties of lunar regolith play a crucial role in influencing the drilling load and coring conditions during the sampling process. To accurately simulate the operational conditions of a coring stem in the lunar environment and obtain reliable experimental data, it is essential to prepare lunar regolith simulants that closely replicate the grain size distribution, physical-mechanical parameters, and mineral composition of actual lunar soil. CSU-LRS-1 is a simulated lunar regolith sample that has been developed based on the physical and mechanical properties, as well as the mineralogical composition, derived from the lunar soil samples returned by the Apollo missions [39].

The lunar regolith returned by the Apollo missions, as analyzed through ground-based experiments, primarily consists of mineral powders, angular fragments, rock debris, and molten glass materials [40,41]. Unlike terrestrial soils, lunar regolith contains a significant amount of molten glass formed by impact processes due to meteoritic collisions. The

particle size distribution is broad, encompassing weathered rock fragments larger than 10 mm as well as fine particles smaller than 0.1 mm [42]. To replicate this composition and particle size distribution, CSU-LRS-1 is synthesized from mineral fragments, angular rock debris, and crystalline rock particles predominantly composed of olivine, plagioclase, pyroxene, ilmenite, and spinel. These components are crushed, ground, and blended, resulting in a particle size distribution ranging from 1 to 1000 microns, closely mirroring that of the Apollo lunar samples.

In addition to particle size distribution, the physical and mechanical properties of the samples play a significant role in determining their core sampling performance. Similar to terrestrial soils, the key parameters include bulk density, relative density, porosity, and the internal friction angle [43]. Furthermore, the density of the soil exhibits substantial variation with depth, which in turn leads to significant differences in shear strength. Based on research reports from the Apollo missions, the depth properties of lunar regolith can be quantified by relative bulk density D_r [44]. Consequently, it is crucial to ensure that the simulated lunar regolith accurately replicates the depth-dependent variations in density and shear strength observed in real lunar regolith. Table 1 compares the key physical and mechanical properties of CSU-LRS-1 with those of the Apollo-returned lunar samples. As shown in the Table 1, the properties of the simulants closely resemble those of the actual lunar regolith.

Table 1. Comparison of CSU-LRS-1 with Apollo samples.

Name	Density (g/cm^3)	Pore Ratio	Specific Gravity	Cohesion (kPa)		Internal Friction Angle (°)	
				D_r = 0.6	D_r = 0.9	D_r = 0.6	D_r = 0.9
CSU-LRS-1	1.49	0.95	2.91	0	4.32	45	49
Apollo Samples	1.43–1.93	0.82–1.17	2.3–3.2	0.41	5.12	42	51

2.1.2. Drilling Experiments

The hollow stem coring method allows for the acquisition of lunar regolith samples that preserve stratigraphic information, making it highly valuable for scientific research. This study investigates the core sampling characteristics of drilling tube-based coring hardware, utilizing the simulated lunar soil sample CSU-LRS-1. The goal is to analyze the influence of drilling parameters on core recovery rates, with the aim of optimizing the drilling process to achieve high core recovery efficiency during lunar exploration.

The experimental platform depicted in Figure 1 is designed to simulate the drilling and sampling process of lunar regolith. The platform, with a total height of approximately 2 m, is divided into two primary sections. The upper section comprises a linear motion lead screw guide, a rotational driving motor, a percussive driving device, a drive gear, and sensors for WOB and torque. This configuration enables linear rotary impact drilling, with the ability to transport the drill pipe over a maximum stroke of 1 m. The lower section houses a cubic frame, within which is a steel container (inner diameter: 45 cm; height: 78 cm) filled with the lunar regolith simulant. The simulant is not stressed by the compaction procedure, and only the self-overburden is considered in this work. This container is securely mounted onto a mobile trolley using bolts and fasteners, facilitating the replacement of the lunar regolith simulant. The trolley can be locked into the cubic frame to ensure stability during operation.

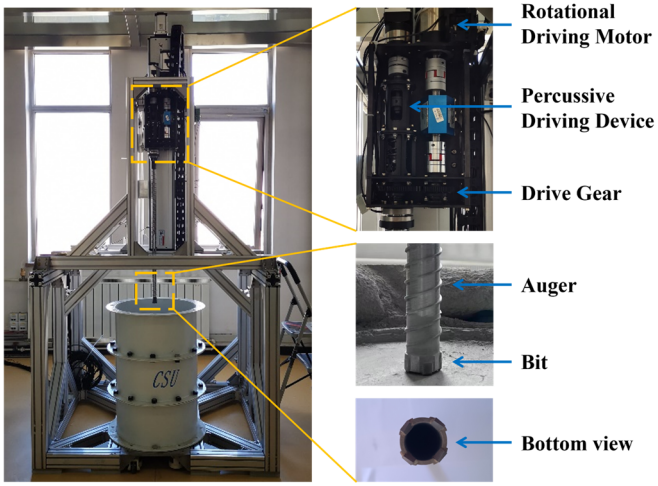


Figure 1. Drilling and coring experimental platform.

Figure 2 illustrates the drilling process. First, the drill bit is positioned at the simulant surface, as shown in Figure 2a. Subsequently, the drilling process begins, with the drill tool operating at a constant penetration speed, rotary speed, and percussive frequency, as depicted in Figure 2b,c. Once the drilling tool reaches the target depth of 350 mm, the penetration, rotation, and impact actions are stopped. Then, the drill pipe is retracted to a predetermined position by the actuator (shown in Figure 2d), and the regolith sample is extracted along with the drill pipe, thus completing the drilling and sampling process. The coring rate is defined as the ratio of the length of the collected lunar soil sample to the drilling depth. In this experiment, a drill pipe with an external spiral structure is utilized, enabling the removal of drilled material through rotational excavation, reducing the required drilling force, and facilitating the penetration of the drill pipe into the lunar regolith.



(a) Initial State (b) Drilling (front view) (c) Drilling (top view) (d) Uplifting Process

Figure 2. Experimental process of drilling and coring.

2.2. Design of Experiments

2.2.1. Taguchi Orthogonal Experiments

This section designs experiments with different combinations of drilling parameters based on the previously described simulated lunar soil sample and drilling experimental platform, providing a data foundation for subsequent coring rate modeling. To ensure that the coring rate model can be effectively applied across the entire control parameter space, the experimental samples must cover as much of the mapping information within this space as possible. However, due to time and labor costs, the number of feasible experiments is limited. Therefore, Design of Experiments (DOE) is needed to obtain as comprehensive and representative samples as possible within the constraints of a limited number of experiments.

The drilling parameters include rotary speed, penetration speed, and percussive frequency. If each parameter is set to 8 levels, a total of 8^3 = 512 experimental combinations would be required, which is impractical. Taguchi orthogonal experiments, based on the principles of mathematical statistics and orthogonal theory, selectively choose representative points from the full experimental space [45,46]. This method ensures comprehensive and uniform coverage while significantly reducing the number of experiments and improving efficiency [38]. Accordingly, this section employs orthogonal experimental design to structure the sampling experiments, with the aim of extracting as much information as possible from the control parameter space within a limited number of trials. The experimental factors and levels are shown in Table 2.

Table 2. The levels of control parameters in drilling experiments.

Drilling Parameters	Level 1	Level 2	Level 3	Level 4	Level 5	Level 6	Level 7	Level 8
Rotary speed (rpm)	80	90	100	110	120	130	140	150
Penetration speed (mm/s)	4	6	8	10	12	13	14	15
Percussive frequency (Hz)	5	10	15	20	25	30	35	40

Orthogonal tables are typically denoted as $L_n(a^p)$, where p factors, each with a levels, are arranged in n experimental runs. The problem addressed in this section involves three factors, each with eight levels. To design the experiments, an $L_{64}(2^5 4^{10} 8^4)$ orthogonal table is employed, resulting in 64 experiments. The distribution of these experiments within the control parameter space is depicted in Figure 3. The colors of the points correspond to the ranges of coring rate value, with darker colors indicating higher coring rates.

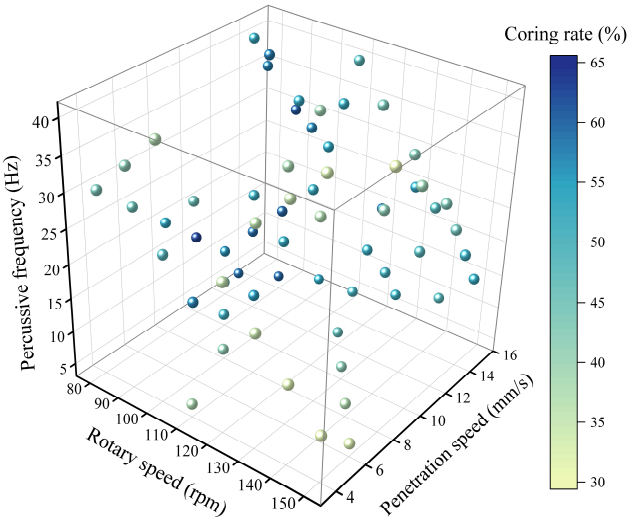


Figure 3. Experimental results of coring rates.

2.2.2. Analysis of Experimental Results

This section examines the influence and underlying trends of drilling parameters on the coring rate, based on the experimental results presented earlier. The effects of each control parameter on the coring rate are assessed through analysis of variance (ANOVA), a statistical method that decomposes the total sum of squares into components attributable to individual factors and their interactions [47,48]. This decomposition allows for the

determination of the significance of each factor's effect on the experimental outcomes. The first column of the table specifies the sources of variation, while the second column presents the sum of squares (SS) associated with each factor. The third column indicates the degrees of freedom (DF); the fourth provides the mean square (MS). The F-value and *p*-value in the fifth and sixth column quantify the degree of influence, with larger F and smaller P indicating greater impact on the results. Specifically, the F-value reflects the ratio of the MS of the parameter (between-group variance) to the MS of error (within-group variance). A higher F-value suggests that the between-group variance is significantly larger relative to the within-group variance, implying that changes in this parameter have a more substantial effect on the outcome. The *p*-value, derived from the F-value and degrees of freedom, determines the statistical significance. Typically, a significance level of 0.05 is used. If the *p*-value is below 0.05, the null hypothesis of the analysis of variance is rejected, indicating that the parameter has a statistically significant impact on the result. Table 3 provides the ANOVA results for the three control parameters and their respective effects on the coring rate. As shown, all three control parameters significantly affect the coring rate, with the degree of influence in descending order: penetration speed, rotary speed, and percussive frequency.

Table 3. ANOVA for coring rate under different drilling parameters.

	SS	DF	MS	*F*	*p*
Rotary speed	0.1611	7	0.0230	32.0179	7.16×10^{-15}
Penetration speed	0.2347	7	0.0335	46.6235	8.74×10^{-18}
Percussive frequency	0.0566	7	0.0081	11.2461	6.36×10^{-8}
Error	0.0302	42	0.0007	-	-
Cor Total	0.4826	63	0.0077	-	-

Additionally, the influence of each control parameter is analyzed using factor level trend plots. In these plots, the factor levels are represented on the *x*-axis, and the experimental outcomes are shown on the *y*-axis, allowing for a direct visualization of the influence and trends of each factor on the results [49]. Figure 4 presents the factor level trend plot for the control parameters and the coring rate. It can be observed that rotary speed negatively impacts the coring rate, penetration speed has a positive effect, and percussive frequency exhibits a non-monotonic relationship, initially increasing and then decreasing the coring rate.

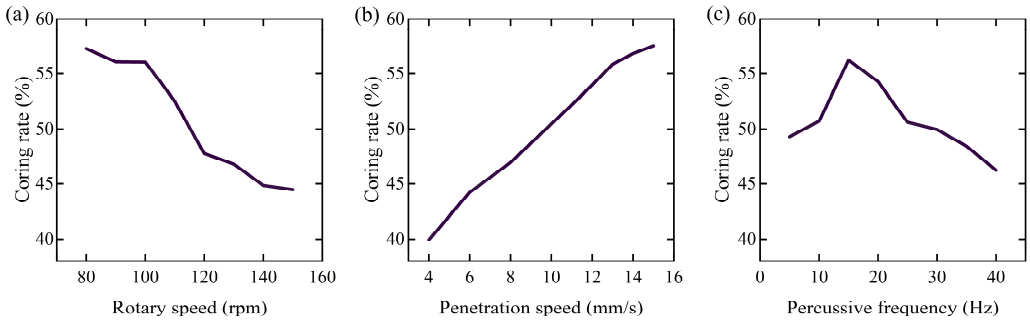


Figure 4. (**a**–**c**) Trend plot of factor levels for drilling parameters and coring rate.

3. Surrogate Model for Coring Efficiency

Surrogate model techniques have emerged as a rapid analytical approach to address challenges like high costs, limited data, and lengthy design cycles in physical experiments for exploring engineering systems' operational behavior. A surrogate model is defined as a

data-driven model constructed with a small number of experimental samples, which approximates the original physical process or simulation calculations [34,50]. The construction of a complete surrogate model involves several steps: experimental design, sample data collection, surrogate model development, accuracy verification, and sequential sampling [51]. Considering the high cost of drilling experiments and the limited availability of sample points, this paper adopts the surrogate modeling approach to establish a mapping relationship between drilling control parameters and coring rate. This surrogate model is used as a substitute and approximation for the original experimental results. Sections 3.1 and 3.2 introduce methods for constructing the surrogate model, while Section 3.3 validates the model based on an independent test set. The modeling process is shown in Figure 5.

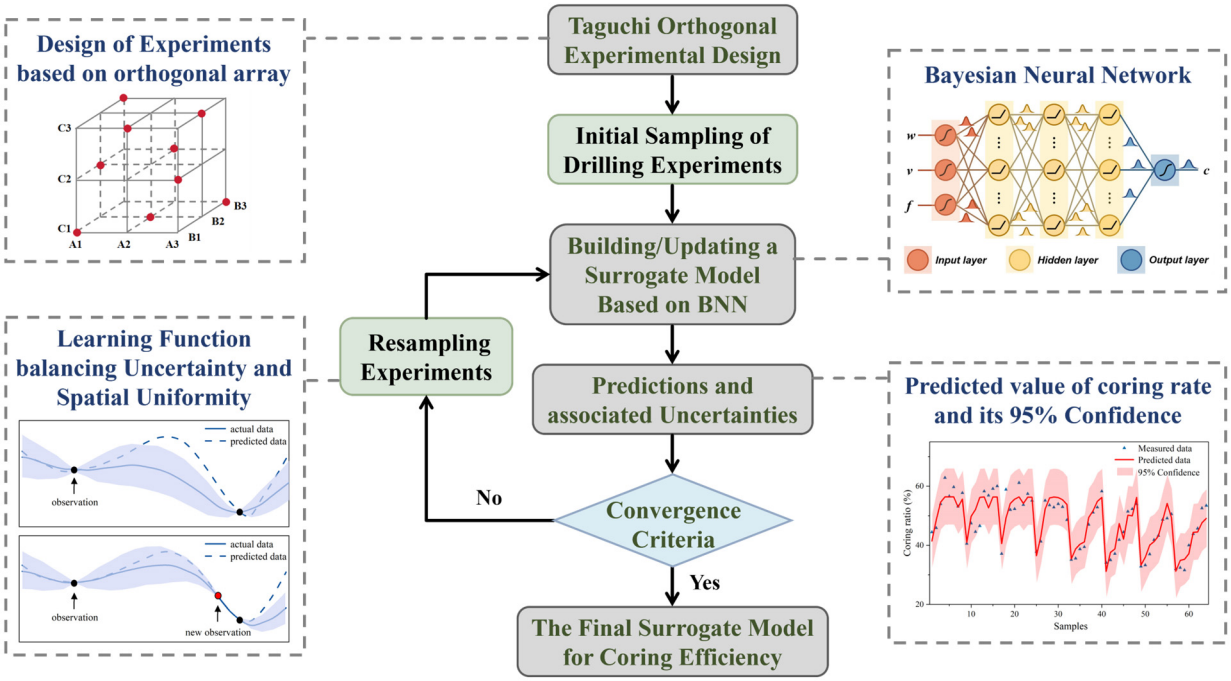


Figure 5. Flowchart of developing a surrogate model for coring efficiency.

3.1. Bayesian Neural Network

This section utilizes the experimental samples from Section 2 to establish a predictive model for the coring rate based on a Bayesian neural network (BNN). A BNN is a model that combines neural networks with Bayesian inference [37]. Unlike traditional neural networks, it treats the weights within the network as probability distributions rather than fixed values, and constructs the model by learning the probability distributions of all parameters [52]. This characteristic enables BNNs to not only provide a predicted value but also offer a measure of uncertainty regarding that prediction [53].

Given that we aim to develop a model that can effectively map the relationship between drilling parameters and coring rate across the entire control parameter space with as few experimental samples as possible, and the initial sample points may not fully capture the mapping information. Therefore, this paper identifies the regions within the BNN with the highest uncertainty based on the initial sample points, performs additional sampling in those regions, and updates the model. This process is repeated iteratively, minimizing the experimental cost while reducing uncertainty in the entire control parameter space to a threshold. Each additional experimental data point maximizes the information gain for the model. The final model gradually approximates the true experimental results and is considered a viable substitute for the original physical model. In summary, the BNN integrates the powerful approximation capabilities of neural networks and the probabilistic

modeling ability of Bayesian inference, enabling it to quantify predictive uncertainties. This makes the BNN particularly well-suited for guiding resampling and addressing the challenges of limited samples and complex systems in this study.

The structure of the BNN constructed in this study is shown in Figure 6. The input layer consists of three nodes, corresponding to the three drilling control parameters of the sampling hardware: rotary speed ω, penetration speed v, and percussive frequency f. The output layer contains a single node, representing the target variable of the model—the coring rate, denoted as c. Due to the relatively small number of input features in this problem, excessively deep or wide networks are prone to overfitting. Therefore, after comparative experiments, a three-layer hidden network is adopted, with 16 neurons in each layer and the activation function set to ReLU. To prevent the model from converging to a local optimum, the RMSprop optimization algorithm combined with an adaptive learning rate decay strategy is used to solve for the model parameters.

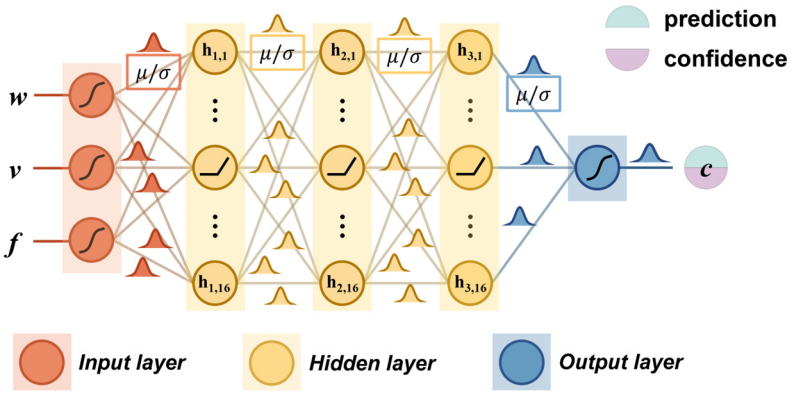


Figure 6. Structure of the Bayesian neural network.

3.2. Active Learning Strategy

3.2.1. Learning Function

Active learning is a strategy that actively selects the most valuable or informative samples for training based on a certain criterion, making it particularly suitable for scenarios where data are expensive or difficult to obtain [36,54]. The uncertainty-based supplementary sampling mentioned earlier is a typical AL strategy [55]. The learning function is the most important evaluation metric in AL methods, used to filter the candidate sample pool and expand the new training set for the surrogate model, thus facilitating the optimization and updating of the model. Generally, the surrogate model reduces uncertainty through resampling and updates, progressively narrowing it to the uncertainty threshold, denoted as ε_U, which is set to 0.05 in this work. However, under limited experimental resources, sampling solely based on uncertainty may lead to the new sampling points clustering in certain regions of the parameter space, causing information redundancy. To maximize the value of each additional experiment, this paper employs the following learning function, as shown in Equation (1), which considers both uncertainty and spatial uniformity during supplementary sampling. This approach strikes a balance between exploring unknown regions and exploiting known information.

$$A(x) = \alpha \cdot U(x) + (1 - \alpha) \cdot D(x) \tag{1}$$

Here, $\alpha \in [0, 1]$ is the weighting factor, $U(x)$ represents the uncertainty of the model's prediction at point x, and $D(x)$ measures the distance between point x and the existing sample points. The uncertainty is quantified by the variance of the prediction distribution, i.e., $U(x) = \sqrt{\sigma^2(x)}$. Spatial uniformity is calculated using the Euclidean distance between

the point to be evaluated and the already sampled points. Let the set of sampled points be $S = \{s_1, s_2, \cdots, s_n\}$, then $D(x) = \min_{s_i \in S} \|x - s_i\|$, where $\|x - s_i\|$ represents the Euclidean distance between the point to be evaluated, x, and a sampled point, s_i. The formula for calculating the Euclidean distance is $\|x - s_i\| = \sqrt{\sum_{j=1}^{3} (x_j - s_{ij})^2}$, where x_j and s_{ij} are the coordinates of points x and s_i in the j-th dimension.

3.2.2. Convergence Criterion

To ensure that the predictive model reaches a stable and accurate state, this study introduces a dual convergence criterion based on both model prediction uncertainty and changes in model predictions. The model is considered converged when both of the following conditions are satisfied. (1) Uncertainty-based Convergence Criterion: The model is considered to have converged in terms of uncertainty when the uncertainty $\mathrm{U(x)}$ of all prediction points in the entire control parameter space χ is below a predefined uncertainty threshold ε_U, i.e., $\forall \mathrm{x} \in \chi, \mathrm{U(x)} \leq \varepsilon_U$, where $\varepsilon_U = 0.05$ in this paper. (2) Model Prediction Change-based Convergence Criterion: The model is considered to have converged in terms of prediction stability when there is no significant change in the predictions across the entire control parameter space between the updated and previous surrogate models, i.e., $\forall \mathrm{x} \in \chi, \frac{\left|\hat{\mathrm{c}}^{(\mathrm{k})} - \hat{\mathrm{c}}^{(\mathrm{k}-1)}\right|}{\hat{\mathrm{c}}^{(\mathrm{k})}} \leq \varepsilon_\Delta$, where $\varepsilon_\Delta = 0.01$ in this paper and $\hat{c}^{(k)}$ represents the prediction of coring rate obtained in the k-th iteration.

3.3. Model Evaluation

To evaluate the prediction accuracy and generalization performance of the constructed model in both interpolation and extrapolation, its performance is measured on an independent test set. The design of the test set should focus on the following key points: First, the test set must be entirely independent from the training set to assess the model's generalization capability on new data. Second, both boundary points and interpolation points within the original parameter range should be included in the test set to examine the model's extrapolation and interpolation abilities. Lastly, to comprehensively assess the model's predictive performance in the control parameter space, the test points should be evenly distributed across the space, providing a more thorough and objective evaluation of the model. Based on these considerations, this section employs an $\mathrm{L_{16}}(4^3)$ orthogonal array for the combination of test set values, ensuring the comprehensiveness and representativeness of the test set despite the limited number of samples. The configuration of the independent test set is shown in Table 4. It is important to note that the surrogate model developed in this study is based on the adjustable parameter space of the drilling device. Therefore, the parameter values in the test set can be freely selected within the adjustable range allowed by the drilling device.

Figure 7 presents the prediction results of the model on the aforementioned independent test set, including predicted values and the 95% confidence intervals. The model makes reasonably accurate predictions for the data in the independent test set, with predicted values being close to the observed values. Furthermore, all observed values fall within the 95% confidence intervals provided by the model. To quantitatively evaluate the model's performance on the test set, a Coefficient of Determination (R^2) and Mean Absolute Percentage Error (*MAPE*) are used, with the formulas for both metrics given in Equations (2) and (3). In these formulas, $\hat{y}_i$ represents the model's predicted value, y_i is the observed value, and n is the number of samples.

$$R^2 = 1 - \frac{\sum_{i=1}^{n} (y_i - \hat{y}_i)^2}{\sum_{i=1}^{n} (y_i - \overline{y})^2} \tag{2}$$

$$MAPE = \frac{1}{n}\sum_{i=1}^{n}\left|\frac{\hat{y}_i - y_i}{y_i}\right| \quad (3)$$

Table 4. Experimental setup for the independent test set.

Samples	Rotary Speed (rpm)	Penetration Speed (mm/s)	Percussive Frequency (Hz)
1	85	5	7.5
2	85	9	17.5
3	85	11	27.5
4	85	14.5	37.5
5	105	5	17.5
6	105	9	7.5
7	105	11	37.5
8	105	14.5	27.5
9	125	5	27.5
10	125	9	37.5
11	125	11	7.5
12	125	14.5	17.5
13	145	5	37.5
14	145	9	27.5
15	145	11	17.5
16	145	14.5	7.5

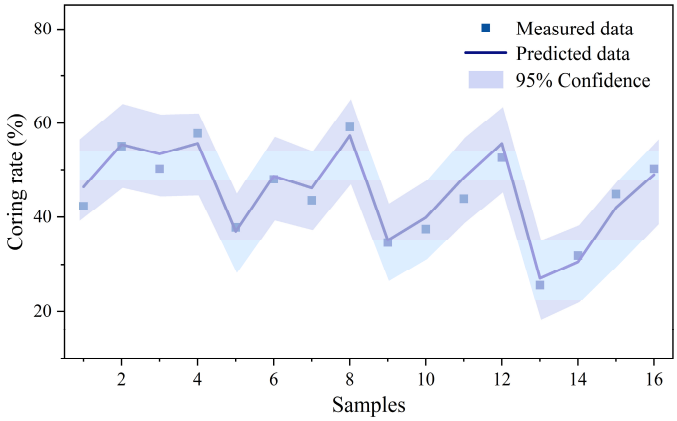


Figure 7. Prediction performance of the surrogate model on the independent test set.

The closer the R^2 value is to 1 and the closer the *MAPE* value is to 0, the better the model's prediction performance. For the independent test set, the model achieved an R^2 of 0.89 and a *MAPE* of 5.74%, further confirming the model's effectiveness and good generalization ability for coring ratio prediction.

Furthermore, a sensitivity analysis of the key hyperparameters of the BNN is conducted to evaluate the robustness of the surrogate model, including the number of hidden layers, the number of neurons per layer, the prior weight coefficient, and the prior variance. The uniqueness of the BNN lies in its use of Bayesian inference, where its loss function incorporates not only the traditional error term but also the log-likelihood term of the prior distribution of weights and biases. The prior weight coefficient controls the proportion of the prior distribution, which is typically modeled as a normal distribution, with the variance characterizing its properties. The value of the R^2 on the independent test is set as a metric for model performance. Figure 8 presents the sensitivity analysis results for the BNN hyperparameters, with each configuration repeated ten times, showing the mean and range of R^2 values. In Figure 8a,b, there is a significant improvement in model performance as the

number of hidden layers and neurons increases initially; however, further increases lead to overfitting, reducing the generalization of the model. In Figure 8c, the model's performance shows an initial increase followed by a decrease as the prior weight changes. A weaker prior causes the model to overly focus on the error term, making it susceptible to noise, whereas a stronger prior leads the model to neglect the data characteristics, hindering its ability to capture data patterns effectively. There exists an optimal prior weight that balances these two influences. Figure 8d demonstrates that there is an optimal value for the variance of the prior distribution, which better aligns with the actual data and helps the model achieve optimal performance. These results indicate that the appropriate selection of BNN hyperparameters is crucial for the model's performance.

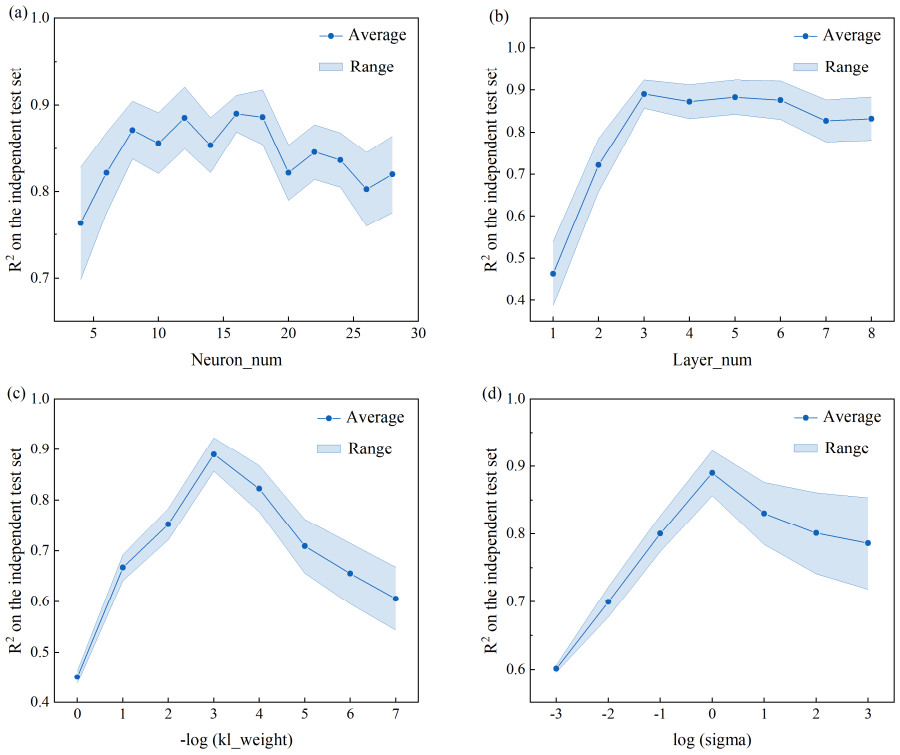


Figure 8. Sensitivity analysis of the hyperparameters in the BNN: (**a**) number of neurons; (**b**) number of hidden layers; (**c**) prior weight coefficient; (**d**) prior variance.

4. Prediction and Discussion

The validation results of the surrogate model on the independent test set, as discussed above, indicate that the model exhibits high extrapolation accuracy and strong generalization capability. Therefore, its results can serve as a substitute for actual experimental outcomes. This section uses the surrogate model to obtain extrapolated and interpolated results for the original experimental points across the entire control parameter space and systematically analyzes the influence of various drilling control parameters on core recovery performance.

4.1. Percussive Effect

Percussion modes play a crucial role in deep drilling and hard rock drilling, with percussive frequency being a key control parameter in these modes. This section uses the previously established surrogate model to study the effect of percussive frequency on the final coring rate, providing scientific guidance for the regulation and optimization of percussive frequency.

4.1.1. Combined Effect of Percussive Frequency and Penetration Speed

This section explores the trend of coring rate variation with percussive frequency at different penetration speeds, while keeping the rotary speed constant. Figure 9 shows the variation in coring rate with percussive frequency when the rotary speed is set to 120 rpm, and the penetration speeds are 6 mm/s, 8 mm/s, 10 mm/s, 12 mm/s, 14 mm/s, and 16 mm/s, respectively. The coring rate initially increases and then decreases as the percussive frequency increases. Furthermore, as the penetration speed increases, the optimal percussive frequency for maximizing the coring rate also increases. Additionally, higher penetration speeds generally lead to higher coring rates.

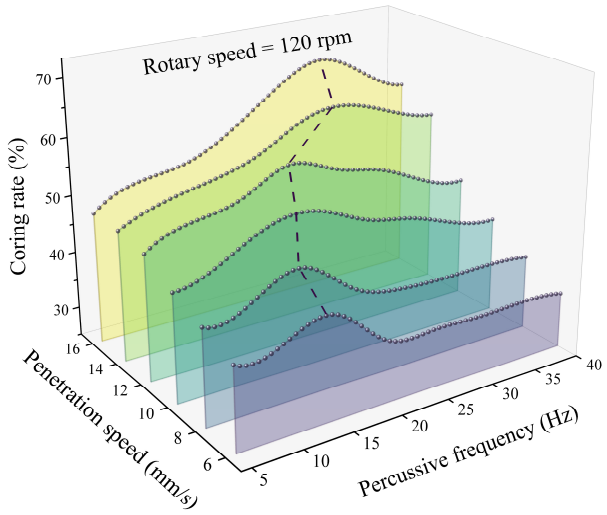


Figure 9. Coring rate vs. percussive frequency curve and comparison at different penetration speeds.

Specifically, the coring rate initially increases and then decreases with the increase in percussive frequency, indicating the existence of an optimal percussive frequency. This behavior may be due to the fact that an appropriate percussive frequency generates sufficient shock forces on the drill pipe, which facilitates regolith loosening and fluidizing, thus enhancing the sampling effect. However, if the percussive frequency is too high, the granular particles may not have fully rebounded before being struck again, which could lead to excessive soil compaction, negatively affecting the sampling process. Additionally, the optimal percussive frequency increases with the penetration speed, meaning that a higher penetration speed requires a higher optimal percussive frequency. This is likely because higher penetration rates necessitate matching higher percussive frequencies to ensure that the shock forces can be effectively applied to the rapidly descending drill pipe, thus maximizing the utilization of percussive energy to overcome soil resistance and improve the coring rate. If the percussive frequency is insufficient, it will fail to meet the sampling demands at high penetration rates, leading to a decrease in the coring rate.

Further results are presented for a low rotary speed (80 rpm) and high rotary speed (150 rpm). As shown in Figure 10, the trends at different rotary speeds reflect the two key patterns mentioned earlier. Additionally, when the rotary speed is low, the optimal percussive frequency increases with ROP, but the change is relatively smaller compared to the higher rotary speed. Higher ROPs are associated with the densification of granular particles, resulting in increased excitation frequency that facilitates the core's entry into the tube.

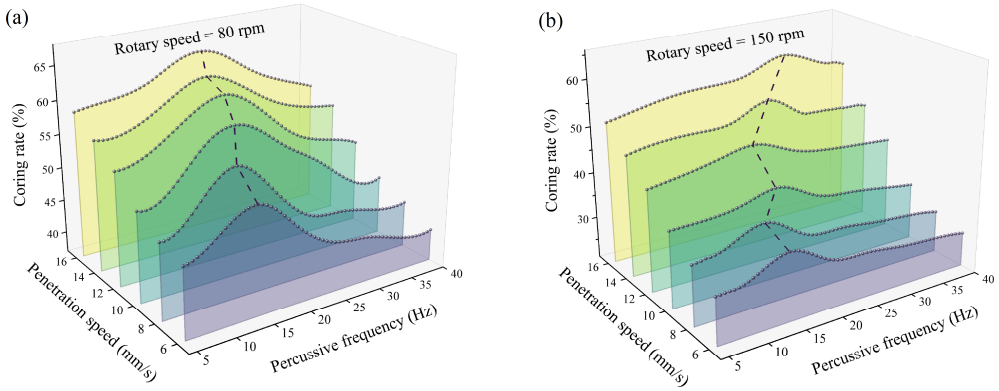


Figure 10. Coring rate vs. percussive frequency curve and comparison at different penetration speeds: (**a**) low rotary speed (80 rpm); (**b**) high rotary speed (150 rpm).

4.1.2. Combined Effect of Percussive Frequency and Rotary Speed

This section explores the trend of the coring rate with percussive frequency at different rotary speeds, while keeping the ROP fixed. Figure 11a–c shows the results for low (4 mm/s), medium (10 mm/s), and high (15 mm/s) ROPs, respectively. It can be observed that, with other parameters fixed, the coring rate initially increases and then decreases with an increase in percussive frequency. Moreover, within each subplot, there is no significant difference in the optimal percussive frequency for different rotary speeds when the ROP is fixed. However, as the ROP increases from Figure 11a–c, the optimal percussive frequency shifts noticeably to the right. Additionally, the coring rate tends to be lower at higher rotary speeds. Higher rotary speeds are associated with the fluidizing of granular particles, which leads to a decrease in excitation frequency, hindering the core's entry into the tube.

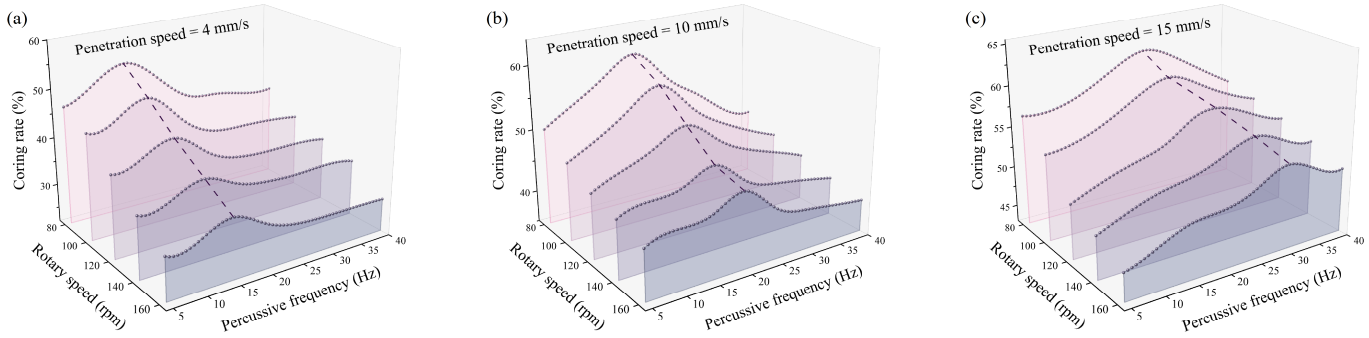


Figure 11. Coring rate vs. percussive frequency curve and comparison at different rotary speeds: (**a**) low penetration speed (4 mm/s); (**b**) medium penetration speed (10 mm/s); (**c**) high penetration speed (15 mm/s).

4.2. Coring Rate and Chip Discharge

The helical-threaded drilling stem transports lunar regolith through external rotational spirals, displacing the advancing space, while the penetration and percussion provide the advancing thrust, thereby enabling the sampling of subsurface lunar regolith. The descent volume of the drill pipe is approximately equal to the sum of the collected and displaced regolith volumes, highlighting the close relationship between coring and chip discharged performance. Based on this correlation, this section investigates the effects of drilling parameters on these two characteristics.

4.2.1. Influence of Rotary and Penetration Speed on Coring Rate

This section investigates the coupled effect of rotary and penetration speed on the coring rate. Figure 12a presents the contour plot of coring rate for different combinations of

rotary speed and penetration speed when the percussive frequency is fixed at 20 Hz. The contour lines exhibit an approximately parallel inclined trend, indicating that, as the rotary speed decreases or the penetration speed increases, the coring rate increases proportionally. Further, the rotary speed and penetration speed are combined into a parameter called the penetration per revolution (*PPR*), defined as Equation (4).

$$PPR = \frac{v}{\omega} \tag{4}$$

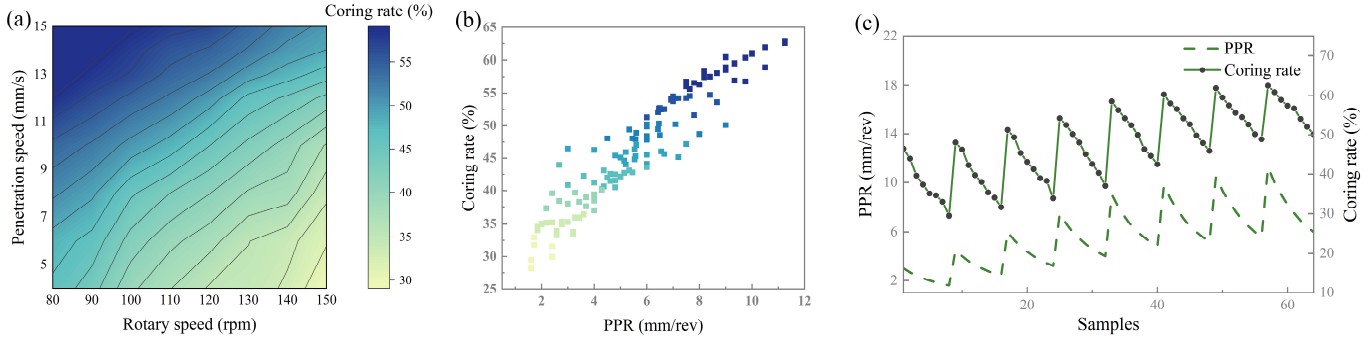


Figure 12. Coupled effect of rotary and penetration speed on coring rate (with percussive frequency fixed at 20 Hz): (**a**) contour plot of coring rate under different rotary and penetration speeds; (**b**) scatter plot of *PPR* versus coring rate; (**c**) variation trend of *PPR* and corresponding coring rate.

Figure 12b shows a scatter plot of *PPR* vs. coring rate, where a near-linear relationship is observed. Figure 12c presents the variation trend of the *PPR* and the corresponding coring rate. It can be seen that the two variables exhibit nearly synchronous fluctuations.

The coring rate is positively correlated with the penetration speed, meaning that, as the penetration speed increases, the coring rate also increases. This can be attributed to the fact that a higher penetration speed provides the drill pipe with stronger penetration capability. Due to the soil's inertial effect, rapid downward movement allows more soil to enter the pipe. Additionally, a higher penetration speed is typically associated with greater drilling pressure, which helps overcome soil resistance and improve the coring rate. However, as the penetration speed continues to increase, the rate of growth in the coring rate starts to flatten. This may be due to the fact that, when the penetration speed becomes too high, the soil may not enter the sampling pipe in time or may become disturbed, causing the increase in coring rate to slow down.

Conversely, the coring rate is negatively correlated with the rotary speed, meaning that a higher rotary speed results in a lower coring rate. The reason for this is that increasing the rotary speed accelerates the cutting action of the drill bit on the soil, causing more soil to be expelled rather than entering the sampling pipe. Therefore, the higher the rotary speed, the more soil is expelled during rotation, which reduces the amount of soil entering the pipe and decreases the coring rate.

The effects of penetration speed and rotation speed on the coring rate exhibit a coupled relationship, which can be measured by *PPR*. Under a fixed percussive frequency, there is an approximately linear relationship between *PPR* and coring rate. *PPR* reflects the coordination between the penetration and rotary speed. This linear relationship between *PPR* and the coring rate may arise from the balanced effect of the penetration rate and rotation speed on the entry of soil into the sampling pipe.

Additionally, Figures 13 and 14 present the cases for low (5 Hz) and high (35 Hz) percussive frequencies. The results also reflect the three key patterns related to penetration speed, rotary speed, and *PPR* mentioned above.

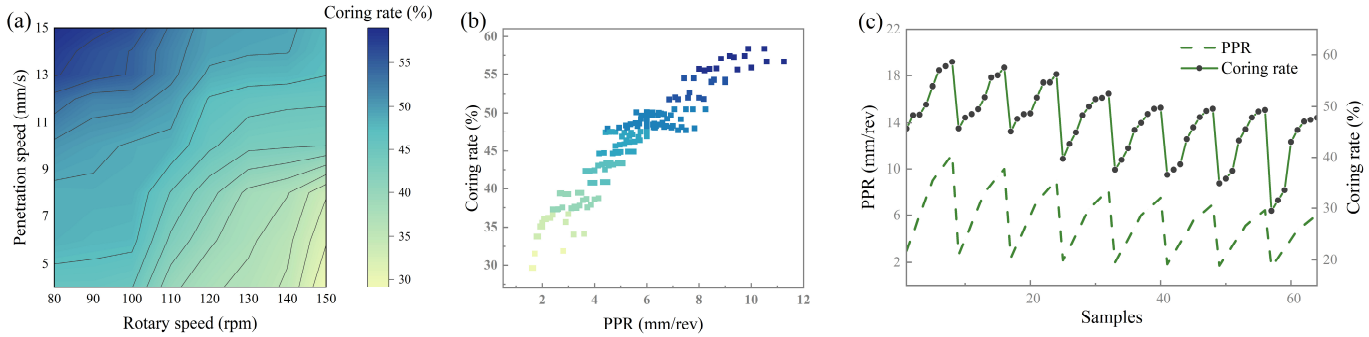


Figure 13. Coupled effect of rotary and penetration speed on coring rate (with percussive frequency fixed at 5 Hz): (**a**) contour plot of coring rate under different rotary and penetration speeds; (**b**) scatter plot of *PPR* versus coring rate; (**c**) variation trend of *PPR* and corresponding coring rate.

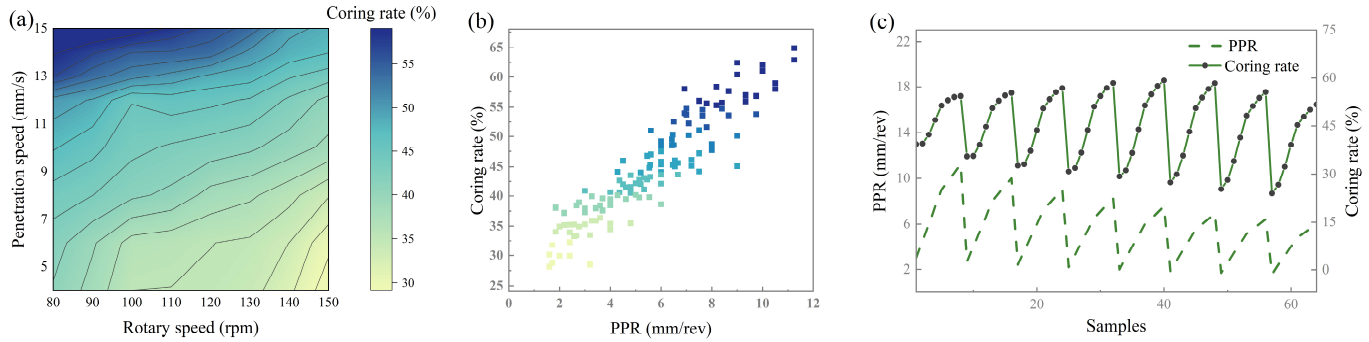


Figure 14. Coupled effect of rotary and penetration speed on coring rate (with percussive frequency fixed at 35 Hz): (**a**) contour plot of coring rate under different rotary and penetration speeds; (**b**) scatter plot of *PPR* versus coring rate; (**c**) variation trend of *PPR* and corresponding coring rate.

4.2.2. Influence of Rotary Speed and Penetration Speed on Chip Discharge

The downward volume of the drill pipe is approximately the sum of the collected and displaced regolith volumes, so the coring rate is closely related to the chip removal performance. During the experimental process, a clear correlation between the volume of removed soil and both rotary speed and penetration speed was observed. Figure 15 shows the variation in the volume of soil removed after drilling under different rotary speeds. The simulated lunar soil ejected from the drilling stem accumulates an approximately conical shape, and its volume (including the diameter and height of the cone's base) increases significantly with higher rotary speeds. This is likely due to the fact that higher rotary speeds result in stronger shear and breaking effects from the drill bit, which fragments the soil, making it more easily expelled and thus creating larger soil piles. Additionally, higher rotary speeds generate significant centrifugal forces, which tend to expel soil from the area around the drill pipe or cutting zone, further increasing the volume of ejected soil. As more soil is expelled, the amount of soil retained inside the pipe decreases, which in turn reduces the core recovery rate. While higher rotary speeds help reduce drilling pressure and promote chip discharge, they are not favorable for improving coring efficiency.

Figure 16 shows the variation in the volume of soil removed after drilling under different penetration speeds. The figure reveals that the soil removal volume significantly decreases as the penetration speed increases. An increase in penetration speed means that the drill bit penetrates the soil layer more quickly, which reduces the time and space available for soil expulsion. Moreover, higher penetration speeds are often accompanied by higher drilling pressures, which help overcome the internal friction of the soil, pushing the soil into the drill pipe and thereby reducing the volume of removed soil and increasing the amount of soil entering the pipe. Based on the analysis above, it can be concluded

that both core recovery and chip removal performance are influenced by the coupling of penetration speed and rotary speed, with penetration speed having a significant impact on coring performance, while rotary speed plays an important role in chip discharge.

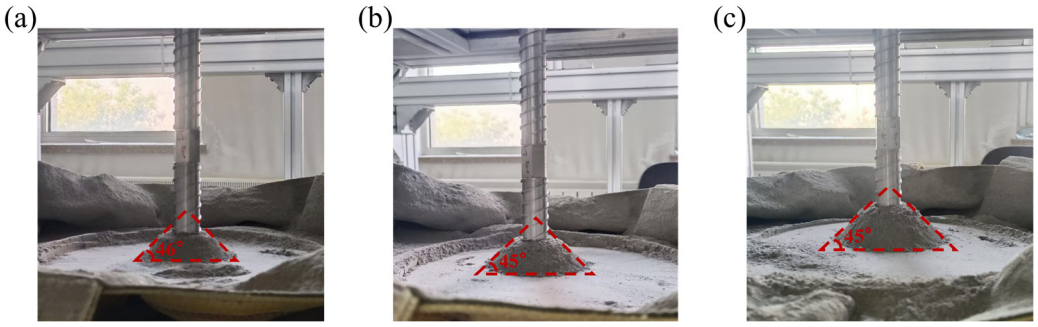


Figure 15. Influence of rotary speed on the volume of chip discharge (v = 8 mm/s, f = 25 Hz): (**a**) w = 90 rpm; (**b**) w = 130 rpm; (**c**) w = 150 rpm.

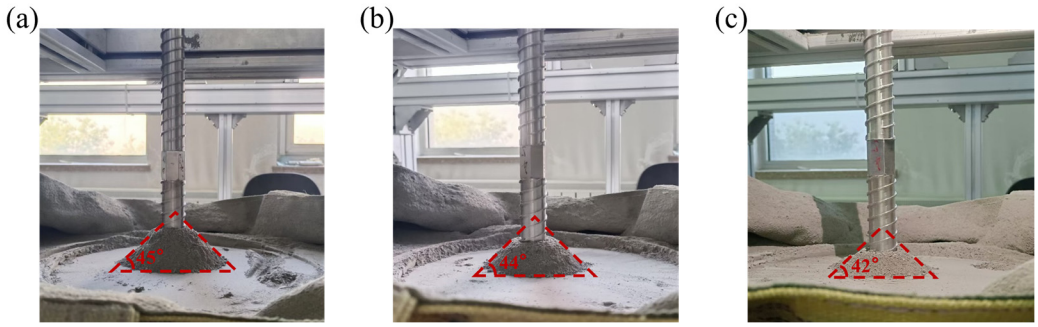


Figure 16. Influence of penetration speed on the volume of chip discharge (w = 130 rpm, f = 20 Hz): (**a**) v = 4 mm/s; (**b**) v = 8 mm/s; (**c**) v = 15 mm/s.

The internal friction angle of soils typically approximates their natural repose angle, increasing with the dense degree [56]. The natural repose angle of the simulated lunar soil, CSU-LRS-1, used in this study is 51° [25]. In Figures 15 and 16, the discharged lunar simulant forms a shape approximately resembling a cone, which accumulates around the drill pipe with an inclination angle of about 45°. This discrepancy may result from the discharged soil undergoing rotational cutting by the drill bit and helical transportation by the drill rod. These processes render the soil looser, thereby reducing its internal friction angle relative to its natural state.

4.3. Optimization of Coring Efficiency

Based on the experimental results and the prediction of surrogate model, the influence of drilling parameters on coring performance can be summarized as follows: The penetration speed exhibits a positive effect on coring efficiency, meaning that, as the penetration speed increases, the coring rate also increases. However, as the penetration speed continues to increase, the rate of growth in coring efficiency begins to level off. The rotary speed has a negative impact on coring efficiency, indicating that lower rotary speeds result in higher coring rates. The effect of percussive frequency on coring efficiency is non-monotonic; namely that the coring rate initially increases and then decreases as the percussive frequency rises. Furthermore, the optimal percussive frequency is dependent on the penetration speed to a large extent, with higher penetration speeds requiring higher optimal percussive frequencies. The optimal frequency typically ranges between 15 and 35 Hz. Consequently, to achieve high coring efficiency, it appears necessary to set a high penetration speed, a low rotary speed, and an appropriate percussion frequency corresponding to the penetration

speed. The response surface of predicted coring rates with different drilling parameters is shown in Figure 17.

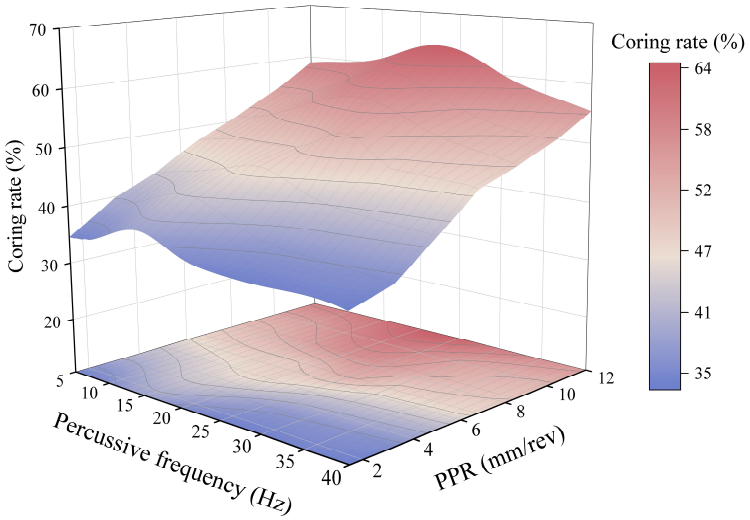


Figure 17. Response surface of predicted coring rates under various drilling parameters.

However, experimental results indicate that the penetration speed positively influences both WOB and torque, while the rotary speed has a negative effect. Specifically, higher penetration speeds and lower rotary speeds result in increased WOB and torque, as illustrated in Figure 18. But, due to the stringent constraints on mass, volume, and available energy imposed by the limited payload capacity of rocket transport systems, the drilling device faces strict limitations on the drilling loads. While high penetration speeds and low rotary speeds can enhance the coring rate, they also demand significantly higher WOB and torque, potentially exceeding the load capacity of the drilling device and diminishing overall drilling efficiency. Thus, it is critical to balance coring efficiency with drilling efficiency, defined as the load and energy required to fracture a unit volume of rock. Optimizing the penetration speed and rotary speed requires careful consideration of this trade-off. Percussion, on the other hand, offers an effective solution by enabling the drill bit to fracture hard rock or loose soil more efficiently. This approach reduces the sustained WOB required, providing a practical means to achieve higher efficiency under constrained load capacities.

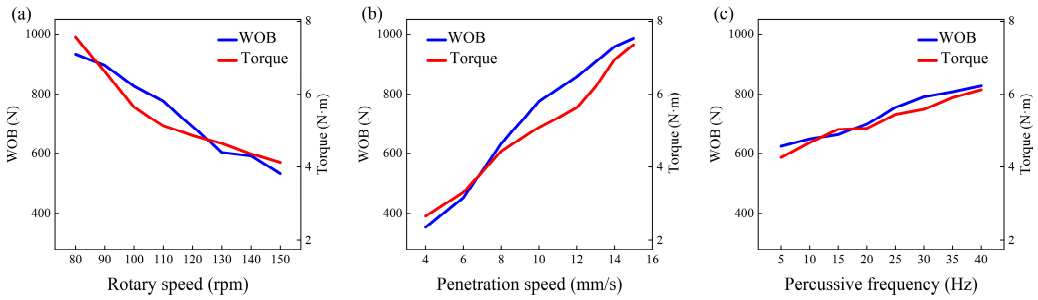


Figure 18. Influence of drilling parameters on WOB and torque: (**a**) rotary speed; (**b**) penetration speed; (**c**) percussive frequency.

5. Conclusions

This paper proposes a surrogate model for drilling and sampling, integrating ground-based experiments and machine learning to serve as an alternative for experimental results. The model is designed to uncover the underlying mechanisms linking drilling parameters and coring performance. First, Taguchi orthogonal experimental design is applied

to collect as comprehensive and representative data as possible within a limited number of trials. Then, a Bayesian neural network is employed to construct a predictive model and quantify uncertainty. Finally, active learning strategies are applied to supplement sampling in regions of high uncertainty, iteratively updating the model to progressively align with real experimental outcomes. This approach significantly reduced the number of experimental samples required to establish a high-fidelity surrogate model. The surrogate model demonstrated strong predictive performance, achieving an R^2 of 0.89 and a *MAPE* of 5.74% on an independent test set, indicating that it effectively captured the intrinsic relationships between drilling parameters and sampling performance, with excellent generalization capability.

Based on the surrogate model, extrapolated and interpolated results are obtained for the original experimental points to investigate the influence mechanisms between drilling parameters and coring performance. The key findings are summarized as follows: (1) Coring rate is positively correlated with penetration speed and negatively correlated with rotary speed. (2) Penetration and rotary speeds have a coupled effect on coring rate, which can be measured by *PPR*, and, when percussive frequency is fixed, the *PPR* exhibits a nearly linear relationship with coring rate. (3) The coring rate increases with percussive frequency, reaches a peak, and then decreases. (4) The optimal percussive frequency increases with penetration speed, meaning that a higher penetration speed requires a higher optimal percussive frequency. These findings provide valuable insights for optimizing drilling parameters to achieve higher coring efficiency and improve the scientific return of lunar missions. The proposed methodology in this paper provides a novel framework for tackling high-cost or small-sample experimental challenges, making it highly valuable for extraterrestrial exploration scenarios. In future work, we will further investigate the effects of geological and drilling tool characteristics on coring results and refine the experimental setup to better simulate lunar gravity and environmental conditions.

Author Contributions: Conceptualization, H.Z., S.L. and Z.Y.; methodology, H.Z., S.L. and Z.Y.; software, S.L. and Z.Y.; validation, S.L., Z.Y., T.D., R.H. and H.Z.; formal analysis, S.L. and Z.Y.; investigation, S.L., Z.Y., T.D. and R.H.; resources, H.Z. and K.W.; data curation, S.L., Z.Y. and H.Z.; writing—original draft preparation, S.L.; writing—review and editing, H.Z., Z.Y. and K.W.; visualization, S.L. and Z.Y.; supervision, H.Z., Z.Y. and K.W.; project administration, H.Z. and K.W.; funding acquisition, H.Z. All authors have read and agreed to the published version of the manuscript.

Funding: H.Z. acknowledges the support from China Manned Space Engineering Program and the Innovative Research Fund of Chinese Academy of Sciences through the Grant No. JCPYJJ-22002.

Data Availability Statement: The datasets generated and supporting the findings of this article are available from the corresponding author upon request.

Acknowledgments: H.Z. sincerely appreciates the insightful discussions with Yewei Zheng from the School of Civil Engineering, Wuhan University.

Conflicts of Interest: The authors declare that they have no known competing financial interests or personal relationships that could have appeared to influence the work reported in this paper.

References

1. Bar-Cohen, Y.; Zacny, K. Drills as Tools for Media Penetration and Sampling. In *Drilling in Extreme Environments: Penetration and Sampling on Earth and other Planets*; Wiley: Hoboken, NJ, USA, 2009; pp. 1–29, ISBN 978-3-527-62662-5.
2. Wei, H.; Zhang, Y.; Zhang, T.; Guan, Y.; Xu, K.; Ding, X.; Pang, Y. Review on Bioinspired Planetary Regolith-Burrowing Robots. *Space Sci. Rev.* **2021**, *217*, 87. [CrossRef]
3. Gorevan, S.; Myrick, T.; Batting, C.; Mukherjee, S.; Bartlett, P.; Wilson, J.F. Strategies for Future Mars Exploration: An Infrastructure for the Near and Longer-Term Future Exploration of the Subsurface of Mars. In Proceedings of the 6th International Conference on Mars, Pasadena, CA, USA, 20–25 July 2003; California Institute of Technology: Pasadena, CA, USA, 2003.

4. Tian, Y.; Tang, D.; Deng, Z.; Jiang, S.; Quan, Q. Drilling Power Consumption and Soil Conveying Volume Performances of Lunar Sampling Auger. *Chin. J. Mech. Eng.* **2015**, *28*, 451–459. [CrossRef]
5. Glass, B.J.; New, M.; Voytek, M.A. Future Space Drilling and Sample Acquisition: A Collaborative Industry-Government Workshop. *Icarus* **2020**, *338*, 113378. [CrossRef]
6. Pitcher, C.; Gao, Y. First Implementation of Burrowing Motions in Dual-Reciprocating Drilling Using an Integrated Actuation Mechanism. *Adv. Space Res.* **2017**, *59*, 1368–1380. [CrossRef]
7. Zacny, K.; Bar-Cohen, Y.; Brennan, M.; Briggs, G.; Cooper, G.; Davis, K.; Dolgin, B.; Glaser, D.; Glass, B.; Gorevan, S.; et al. Drilling Systems for Extraterrestrial Subsurface Exploration. *Astrobiology* **2008**, *8*, 665–706. [CrossRef]
8. Gromov, V.; Misckevich, A.V.; Vidkin, E.N.; Kochan, H.W.; Coste, P.; Re, E. The Mobile Penetrometer, a "Mole" for Sub-Surface Soil Investigation. In Proceedings of the 7th European Space Mechanisms and Tribology Symposium, Noordwijk, The Netherlands, 1–3 October 1997.
9. Shi, X.-M.; Jie, D.-G.; Quan, Q.; Tang, D.-W.; Jiang, S.; Deng, Z. Experimental Research on Lunar Soil Simulant Drilling Load Analysis. *Yuhang Xuebao/J. Astronaut.* **2014**, *35*, 648–656. [CrossRef]
10. Quan, Q.; Tang, J.; Jiang, S.; Deng, Z.; Guo, H.; Tao, Y. A Real-Time Recognition Based Drilling Strategy for Lunar Exploration. In Proceedings of the 2014 IEEE/RSJ International Conference on Intelligent Robots and Systems, Chicago, IL, USA, 14–18 September 2014; pp. 2375–2380.
11. Prissel, T.C.; Prissel, K.B. A Lunar Sample Renaissance. *Nat. Commun.* **2021**, *12*, 7053. [CrossRef]
12. Armarego, E.J.A.; Smith, A.J.R.; Karri, V. Mechanics of Cutting Model for Simulated Oblique Rotary Tool Cutting Processes. *J. Mater. Process. Technol.* **1991**, *28*, 3–14. [CrossRef]
13. Yu, Y.; Arnold, P.C. Theoretical Modelling of Torque Requirements for Single Screw Feeders. *Powder Technol.* **1997**, *93*, 151–162. [CrossRef]
14. Chen, T.; Zhao, Z.; Wang, Q.; Wang, Q. Modeling and Experimental Investigation of Drilling into Lunar Soils. *Appl. Math. Mech.* **2019**, *40*, 153–166. [CrossRef]
15. Wang, Z.; Li, J.; Yu, T.; Cheng, Q.; Li, F.; Li, Z. Sampling Dynamic Analysis and Discrete Element Simulation on a Deep Layer Regolith Drill for Extraterrestrial Celestial Bodies. *Acta Astronaut.* **2024**, *225*, 141–157. [CrossRef]
16. Tong, L.; Zhao, D.; Hu, M.; Gao, X.; Wang, H. Drilling and Migration Characteristics of Critical Size Lunar Soil Particles. *IOP Conf. Ser. Mater. Sci. Eng.* **2020**, *926*, 012021. [CrossRef]
17. Liu, T.; Zhou, J.; Liang, L.; Zhao, Y.; Cao, D. A Novel Torque Analysis Method for Drilling Deep Lunar Soil by DEM. *J. Terramechanics* **2021**, *94*, 23–37. [CrossRef]
18. Roberts, I.P.I. Determination of the Vertical and Lateral Pressures of Granular Substances. *Proc. R. Soc. Lond.* **1883**, *36*, 225–240.
19. Nagaoka, K.; Kubota, T.; Otsuki, M.; Tanaka, S. Experimental Study on Autonomous Burrowing Screw Robot for Subsurface Exploration on the Moon. In Proceedings of the 2008 IEEE/RSJ International Conference on Intelligent Robots and Systems, Nice, France, 22 September 2008; pp. 4104–4109.
20. Tang, J.; Chen, X.; Zhang, H.; Tian, Y.; Zhang, W.; Jiang, S.; Deng, Z. Soil Flowing Characteristics during Flexible Tube Coring for Lunar Exploration: Modeling and Verification. *Acta Astronaut.* **2023**, *212*, 387–397. [CrossRef]
21. Tang, J.; Quan, Q.; Jiang, S.; Li, H.; Bai, D.; Tang, D.; Deng, Z. Experimental Investigation on Flowing Characteristics of Flexible Tube Coring in Lunar Sampling Missions. *Powder Technol.* **2018**, *326*, 16–24. [CrossRef]
22. Zhang, K.; Xuyan, H.; Pan, W.; Ding, T.; Deng, Z. The Study of the Drilling Core Features of a Multi-Pipe Deep Lunar Soil Sampling Driller for Manned Lunar Exploration Based on the Discrete Element Technology. In Proceedings of the 2015 IEEE International Conference on Robotics and Biomimetics (ROBIO), Zhuhai, China, 6–9 December 2015; p. 2346.
23. Wang, Y.; Zheng, D.; Yin, Z.; Zhang, W.; Zu, L.; Tao, G.; Yu, S. Research on Chip Removal Performance of Rotary Percussive Ultrasonic Drill for Planetary Rock Sampling. *Aerospace* **2024**, *11*, 831. [CrossRef]
24. Zacny, K.; Cooper, G.A. Methods for Cuttings Removal from Holes Drilled on Mars. *Int. J. Mars Sci. Explor.* **2007**, *3*, 42–56. [CrossRef]
25. Yuan, Z.; Zhao, H.; Li, X.; Ning, Z.; Wang, Z.; Mu, R.; Wang, K. Design and Modeling of a Dual-Archimedes Screw Deep Drilling System for Lunar Subsurface Exploration. *Acta Astronaut.* **2024**, *217*, 221–237. [CrossRef]
26. Gao, Y.; Frame, T.E.; Pitcher, C. Peircing the Extraterrestrial Surface: Integrated Robotic Drill for Planetary Exploration. *IEEE Robot. Autom. Mag.* **2015**, *22*, 45–53. [CrossRef]
27. Boukredera, F.S.; Youcefi, M.R.; Hadjadj, A.; Ezenkwu, C.P.; Vaziri, V.; Aphale, S.S. Enhancing the Drilling Efficiency through the Application of Machine Learning and Optimization Algorithm. *Eng. Appl. Artif. Intell.* **2023**, *126*, 107035. [CrossRef]
28. Hao, J.; Xu, H.; Peng, Z.; Cao, Z. An Online Adaptive ROP Prediction Model Using GBDT and Bayesian Optimization Algorithm in Drilling. *Geoenergy Sci. Eng.* **2025**, *246*, 213596. [CrossRef]
29. Yang, Y.; Cen, X.; Ni, H.; Liu, Y.; Chen, Z.J.; Yang, J.; Hong, B. A Highly Accurate and Robust Prediction Framework for Drilling Rate of Penetration Based on Machine Learning Ensemble Algorithm. *Geoenergy Sci. Eng.* **2025**, *244*, 213423. [CrossRef]

30. Bizhani, M.; Kuru, E. Towards Drilling Rate of Penetration Prediction: Bayesian Neural Networks for Uncertainty Quantification. *J. Pet. Sci. Eng.* **2022**, *219*, 111068. [CrossRef]
31. Xu, J.; Yuan, X.; Zhang, Y.; Yu, S.; Pang, Y.; Zhang, T.; Xu, K.; Ding, X. Real-Time Prediction of Drilling Forces inside Lunar Regolith Based on Recurrent Neural Networks. *Acta Astronaut.* **2022**, *201*, 259–273. [CrossRef]
32. Xu, J.; Liu, J.; Yu, S.; Xu, K.; Zhang, T. Real-Time Temperature Prediction of Lunar Regolith Drilling Based on ATT-Bi-LSTM Network. *Int. J. Heat Mass Transf.* **2024**, *218*, 124783. [CrossRef]
33. Chen, D.; Lv, P.; Xue, L.; Xing, H.; Lu, L.; Kong, D. Positional Error Compensation for Aviation Drilling Robot Based on Bayesian Linear Regression. *Eng. Appl. Artif. Intell.* **2024**, *127*, 107263. [CrossRef]
34. Koziel, S.; Leifsson, L. Introduction to Surrogate Modeling and Surrogate-Based Optimization. In *Simulation-Driven Design by Knowledge-Based Response Correction Techniques*; Koziel, S., Leifsson, L., Eds.; Springer International Publishing: Cham, Switzerland, 2016; pp. 31–61, ISBN 978-3-319-30115-0.
35. Zhang, J.; Zhang, K.; Liu, P.; Zhang, L.; Fu, W.; Chen, X.; Wang, J.; Liu, C.; Yang, Y.; Sun, H.; et al. Deep Bayesian Surrogate Models with Adaptive Online Sampling for Ensemble-Based Data Assimilation. *J. Hydrol.* **2025**, *649*, 132457. [CrossRef]
36. Tong, S. *Active Learning: Theory and Applications*; Stanford University: Stanford, CA, USA, 2001.
37. Lampinen, J.; Vehtari, A. Bayesian Approach for Neural Networks—Review and Case Studies. *Neural Netw.* **2001**, *14*, 257–274. [CrossRef] [PubMed]
38. Freddi, A.; Salmon, M. Introduction to the Taguchi Method. In *Design Principles and Methodologies: From Conceptualization to First Prototyping with Examples and Case Studies*; Freddi, A., Salmon, M., Eds.; Springer International Publishing: Cham, Switzerland, 2019; pp. 159–180, ISBN 978-3-319-95342-7.
39. Wu, Q.; Jia, Y.; Wu, H.; Yuan, Z.; Tang, X.; Zheng, Y.; Zhao, H. Macro- and Micro-Mechanical Behavior of CSU-LRS-1 Lunar Soil Simulant under True Triaxial Loading Path. *Granul. Matter* **2024**, *26*, 63. [CrossRef]
40. Mitchell, J.K.; Houston, W.N.; Scott, R.F.; Costes, N.C.; Carrier, W.D.; Bromwell, L.G. Mechanical Properties of Lunar Soil—Density, Porosity, Cohesion, and Angle of Internal Friction. *Proc. Lunar Sci. Conf.* **1972**, *3*, 3235.
41. Zhao, J.; Huang, J.; Qiao, L.; Xiao, Z.; Huang, Q.; Wang, J.; He, Q.; Xiao, L. Geologic Characteristics of the Chang'E-3 Exploration Region. *Sci. China Phys. Mech. Astron.* **2014**, *57*, 569–576. [CrossRef]
42. Anand, M.; Crawford, I.A.; Balat-Pichelin, M.; Abanades, S.; van Westrenen, W.; Péraudeau, G.; Jaumann, R.; Seboldt, W. A Brief Review of Chemical and Mineralogical Resources on the Moon and Likely Initial in Situ Resource Utilization (ISRU) Applications. *Planet. Space Sci.* **2012**, *74*, 42–48. [CrossRef]
43. Zheng, Y.-C.; Ouyang, Z. Physical and mechanical properties of lunar regolith. *J. Mineral. Petrol.* **2004**, *24*, 14–19.
44. Yuan, Z.; Zhao, H. Towards Ultra-Deep Exploration in the Moon: Modeling and Implementation of a Mole-Type Burrowing System. In Proceedings of the the 57th U.S. Rock Mechanics/Geomechanics Symposium, Atlanta, GA, USA, 25 June 2023; p. ARMA-2023-0174.
45. Kacker, R.N.; Lagergren, E.S.; Filliben, J.J. Taguchi's Orthogonal Arrays Are Classical Designs of Experiments. *J. Res. Natl. Inst. Stand. Technol.* **1991**, *96*, 577–591. [CrossRef] [PubMed]
46. Roy, R.K. *Design of Experiments Using The Taguchi Approach: 16 Steps to Product and Process Improvement*; John Wiley & Sons: Hoboken, NJ, USA, 2001.
47. St»hle, L.; Wold, S. Analysis of Variance (ANOVA). *Chemom. Intell. Lab. Syst.* **1989**, *6*, 259–272. [CrossRef]
48. Sawyer, S.F. Analysis of Variance: The Fundamental Concepts. *J. Man. Manip. Ther.* **2009**, *17*, 27E–38E. [CrossRef]
49. Lazic, L. Use of Orthogonal Arrays and Design of Experiments via Taguchi Methods in Software Testing. *Recent Adv. Appl. Theor. Math.* **2013**, *23*, 256–267.
50. Tripathy, R.K.; Bilionis, I. Deep UQ: Learning Deep Neural Network Surrogate Models for High Dimensional Uncertainty Quantification. *J. Comput. Phys.* **2018**, *375*, 565–588. [CrossRef]
51. Ponweiser, W.; Wagner, T.; Vincze, M. Clustered Multiple Generalized Expected Improvement: A Novel Infill Sampling Criterion for Surrogate Models. In Proceedings of the 2008 IEEE Congress on Evolutionary Computation (IEEE World Congress on Computational Intelligence), Hong Kong, China, 1 June 2008; pp. 3515–3522.
52. Heckerman, D. Bayesian Networks for Data Mining. *Data Min. Knowl. Discov.* **1997**, *1*, 79–119. [CrossRef]
53. Bielza, C.; Larrañaga, P. Bayesian Networks in Neuroscience: A Survey. *Front. Comput. Neurosci.* **2014**, *8*, 131. [CrossRef]
54. Ren, P.; Xiao, Y.; Chang, X.; Huang, P.-Y.; Li, Z.; Gupta, B.B.; Chen, X.; Wang, X. A Survey of Deep Active Learning. *ACM Comput. Surv.* **2021**, *54*, 1–40. [CrossRef]

55. van Hout-Wolters, B.; Simons, R.-J.; Volet, S. Active Learning: Self-Directed Learning and Independent Work. In *New Learning*; Simons, R.-J., van der Linden, J., Duffy, T., Eds.; Springer: Dordrecht, The Netherlands, 2000; pp. 21–36, ISBN 978-0-306-47614-3.
56. Beakawi Al-Hashemi, H.M.; Baghabra Al-Amoudi, O.S. A Review on the Angle of Repose of Granular Materials. *Powder Technol.* **2018**, *330*, 397–417. [CrossRef]

Disclaimer/Publisher's Note: The statements, opinions and data contained in all publications are solely those of the individual author(s) and contributor(s) and not of MDPI and/or the editor(s). MDPI and/or the editor(s) disclaim responsibility for any injury to people or property resulting from any ideas, methods, instructions or products referred to in the content.